Thin-film flows with moving contact lines: An approach to reducing computing time

J. M. Gomba*

Department of Mechanical Engineering, University of California at Santa Barbara, Santa Barbara, California 19327, USA

(Received 3 October 2011; published 8 May 2012)

A numerical method to reduce the computing times of thin-film flows with moving contact lines is presented. The flows of a film and a droplet are calculated in a frame that moves with a nonconstant velocity $U(t)$. The criterion employed to define this velocity is to reduce the maximum height change in the flow's most critical zone. The efficiency of the algorithm in reducing the CPU time is tested in gravity-driven flows, where the computing time is reduced by up to a factor of 13 depending on the parameters of the problem.

DOI: 10.1103/PhysRevE.85.056701 PACS number(s): 47.11.Bc, 47.15.gm

I. INTRODUCTION

Thin-film flows are ubiquitous in both technological applications and in nature, e.g., in coating processes, flows in micrometric devices, thin films in mammalian lungs, etc. [1–7]. In order to understand the film dynamics in different scenarios and to improve the efficiency of technological processes and microfluidic devices, the numerical study of thin films has been expanding and a large number of papers devoted to this issue have been published over the past two decades (see [8,9] and the citations therein). Nevertheless, and despite all the work done, the numerical simulation of thin-film flows with moving contact lines is still very time-consuming.

The most popular approach to modeling thin-film flows is the use of a lubrication framework. A semi-implicit time-splitting technique and an alternating-direction implicit (ADI) scheme are usually employed to solve the resulting fourth-order partial differential equation [10,11]. This framework combines some of the stability properties of implicit schemes with the cost efficiency of explicit ones.

The computation of thin-film flows presents by far the most important difficulties in the region close to the advancing contact line. In this region, the thickness profile adopts an oscillatory structure that penetrates into the precursor film [12]. Despite the fact that the size of this region is very small when compared to the typical extension of the flow, the dynamics at the contact line has an important effect on the bulk flow. For example, the velocity in this region presents a step profile that is responsible for the stability of the flow [13–15] and, thus, the front requires a very dense mesh in order to solve the whole flow with good accuracy. On the other hand, when the fluid has moving contact lines, the domain must be large enough to allow the description of the flow along all its evolution. Therefore, the need to use extended domains and small cell sizes, such as that required in the contact line region, greatly increases the computational time needed to solve the flow.

Under pinned contact line conditions, it is possible to use a nonuniform mesh in the critical region [16]. In problems that involve moving contact lines, it is possible to employ an adaptive grid, where the number and size of the elements of the mesh is modified as the flow evolves. The most difficult issue with this method is to define a monitor function that efficiently controls the size of the cells without losing precision [17,18]. Gaskell and his collaborators have done much to develop this approach and to use it to understand fundamental aspects of droplet spreading. They successfully implemented fully implicit multigrids with an adaptive time-stepping lubrication solver to study the flow of droplets on chemically and topographically heterogeneous surfaces [19–21].

Here, an alternative technique to solve thin-film flows with moving contact lines is presented. This algorithm solves the thickness equation in a moving frame, allowing an easy use of nonuniform meshes. The velocity of the frame is calculated in each temporal step to reduce the maximum of the velocity field u at the contact line region, so the most critical region is solved in a quasisteady frame.

This text is organized as follows. In Sec. II, the lubrication framework is presented. Section III is devoted to the presentation of the numerical method and related issues. The benchmark problem, the constant flow (CF) case, is analyzed in Sec. IV. This case is particularly interesting because it admits a traveling-wave solution that moves with a velocity that can be analytically predicted. The thickness profiles obtained by solving the flow in a moving frame on a nonuniform grid are compared with the profiles obtained by simulating the same case on a uniform grid in a laboratory frame. The corresponding CPU times are also compared. In Sec. V, an analog analysis is performed for the flow of a droplet, which is an example of a constant volume (CV) flow. Contrary to the CF case, the velocity of the droplet does not admit a traveling-wave solution and there is no frame in which the thickness profile is steady. Finally, the conclusions are presented in Sec. VI.

II. FORMULATION

Thin-film flows are usually studied within the lubrication approximation, i.e., assuming small free surface slopes and negligible Reynolds number. A major hindrance in the development of the theory for film flows is the incomplete knowledge of the physics at the contact line [9]. When the nonslip boundary condition at the fluid-solid interface is imposed, a multivalued fluid velocity appears at the moving contact line and the shear stress diverges as the fluid thickness goes to zero. Here, this singularity is overcome by including a microscopic precursor film ahead of the apparent contact line [14,22].

*Present address: Instituto de Física Arroyo Seco, Universidad Nacional del Centro de la Provincia de Buenos Aires, Pinto 399, 7000 Tandil, Argentina; jgomba@engr.ucsb.edu

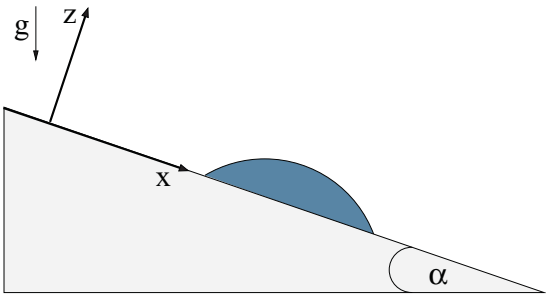

FIG. 1. (Color online) Sketch of a droplet spreading down an inclined plane.

Let us consider a two-dimensional flow that advances in the $\tilde{x}$ direction with at least one moving contact line, as shown in Fig. 1. The equation of continuity for a film with thickness $\tilde{h}$, measured in the $\tilde{z}$ direction, is solved in a frame that moves in the $\tilde{x}$ direction with a velocity $\tilde{U}(t)$ ($\tilde{U}=0$ corresponds to the laboratory frame). The general form of this equation is [15]

$$\frac{\partial \tilde{h}}{\partial \tilde{t}} + \frac{\partial}{\partial \tilde{x}}[(\bar{\tilde{u}} - \tilde{U})\tilde{h}] = 0, \tag{1}$$

where $\bar{\tilde{u}}(x,t)$ is the mean velocity, given by

$$\bar{\tilde{u}} = \frac{1}{\tilde{h}} \int_0^{\tilde{h}} \tilde{u}\, d\tilde{z}, \tag{2}$$

$\tilde{u}(x,z,t)$ being the velocity in the $\tilde{x}$ direction.

The expression for $\bar{\tilde{u}}$ depends on the problem at hand. Here, the algorithm is tested on gravity-driven flows. In particular, we consider a (constant or nonconstant) volume of fluid spreading down an inclined plane, for which the velocity is given by

$$\bar{\tilde{u}} = -\frac{\tilde{h}^2}{3\mu}\left[\frac{\partial}{\partial \tilde{x}}(\rho g \cos\alpha \tilde{h} - \gamma \nabla^2 \tilde{h}) - \rho g \sin\alpha\right], \tag{3}$$

where α is the inclination angle of the substrate, g is the gravity, and μ, ρ, γ are the viscosity, density, and surface tension, respectively.

It is convenient to solve the problem in dimensionless variables, so we define $\tilde{x} = x_c\, x$, $\tilde{h} = h_c\, h$, $\tilde{t} = t_c\, t$ (x_c, h_c, and t_c being the typical lengths and temporal scale of the problem, respectively), and $\tilde{U} = t_c/x_c\, U$. Thus, the dimensionless form for Eq. (1) is

$$\frac{\partial h}{\partial t} = -(h^3 h_{xxx})_x - G_{\parallel}(h^3)_x + G_{\perp}(h^3 h_x)_x + U h_x. \tag{4}$$

Here t, x, and $h(x,t)$ are dimensionless and t_c is

$$t_c = \frac{3\mu}{\gamma}\frac{x_c^4}{h_c^3}. \tag{5}$$

Equation (4) has two dimensionless parameters that depend on the scales x_c and h_c in the following form:

$$G_{\perp} = \frac{x_c^2}{a^2}\cos\alpha, \quad G_{\parallel} = \frac{x_c^3}{h_c a^2}\sin\alpha, \tag{6}$$

$a = \sqrt{\gamma/(\rho g)}$ being the capillary length. Up to this point, x_c and h_c are not yet specified. The definition of both scales depends strongly on the problem to be solved. For example, when a constant flow (CF) is imposed at the beginning of the domain, h_c is chosen to be the resulting constant thickness of the film at that point [15,23]. When, instead, a constant volume (CV) of fluid is considered, the capillary length or the initial maximum thickness are usually employed [5,24]. We will appropriately define the corresponding scales in the following sections.

III. NUMERICAL ISSUES

Each term of Eq. (4) is discretized employing a centered finite-difference scheme. Thus, the temporal derivative $\partial h_i/\partial t$ is coupled with the h_{i-j} neighbor values, with $j = -2, -1, 0, 1$, and 2, which results in the following system of equations:

$$\frac{\partial h_i}{\partial t} = -f_i, \tag{7}$$

with f_i given by

$$f_i = \sum_{j=-2}^{2} a_{i,i-j} h_{i-j}. \tag{8}$$

and $i = 1, \ldots, N$. Here, $a_{i,i-j}$ is a pentadiagonal matrix with nonzero elements depending on the coefficients of Eq. (4) and on the cell size Δx_{i-j}. In order to preserve the positivity of the solution, we employ a positivity-preserving scheme (PPS) [25–27] to discretize the diffusion $D(h) = h^3$ of the capillary term [16]:

$$D(h_i) = \begin{cases} \frac{h_i - h_{i-1}}{-2h_i^2 + 2h_{i-1}^2} & \text{for} \quad h_i \neq h_{i-1}, \\ h_{i-1}^3 & \text{for} \quad h_i = h_{i-1}. \end{cases}$$

The system of Eq. (7) evolves in time using a Crank-Nicholson scheme, that is,

$$\frac{h_i^{n+1} - h_i^n}{\Delta t^n} = -1/2\left(f_i^{n+1} + f_i^n\right). \tag{9}$$

Equation (9) is solved by using a Newton-Kantorovich method. Briefly, we write h_i^{n+1} as

$$h_i^{n+1} = h_i^* + q_i^n, \tag{10}$$

h_i^* being a guess (usually $h_i^* = h_i^n$) and q_i^n unknown. The quantity f_i^{n+1} is written as

$$f_i^{n+1} = f_i^* + F_{i,l}^*\, q_l^n, \tag{11}$$

where

$$F_{i,l}^* = \left.\frac{\partial f_i}{\partial q_l}\right|^* \tag{12}$$

is the Jacobian matrix and the asterisk indicates evaluation using the guess h_i^*. Thus, Eq. (9) is written in the following form:

$$(\delta_{i,l} + \theta \Delta t^n F_{i,l}^*) q_l^n = h_i^n - h_i^* - (1-\theta) f_i^n - \theta \Delta t^n f_i^*, \tag{13}$$

where $\delta_{i,l}$ is the Kronecker delta. This system of equations for the correction q_i^n is solved by using the well known routines BANDEC and BANBKS [28].

After each temporal step, the difference $\bar{u}_i' = \bar{u}_i - U$ is solved, $\bar{u}_i'$ being the flow velocity measured on the moving frame. In order to solve Eq. (1) at t^n, the velocity $U(t^{n-1})$ is employed. The velocity of the moving frame is calculated for each temporal step by following this simple but effective

algorithm:

$$U(t^n) = U(t^{n-1}) + \max_{1<i<N}[\bar{u}_i'(t^n)], \tag{14}$$

with $U(0) = 0$. In general, the maximum velocity occurs in the ridge region (or "bump") that develops close to the contact line, the most critical region of the flow. The key idea in this definition is to solve this crucial zone in a quasisteady frame, reducing the rate of change of the thickness and thus allowing for an increase in the temporal step Δt. In addition, numerical calculations show that with this definition of U, the contact line stays almost in the same region of the numerical domain, allowing smaller values of Δx in this region and larger in the rest of the grid.

A. Meshing the domain

The length L of the numerical domain is divided into N cells of width Δx_i, the size of each cell being a smooth function of its position. The parameters of this function are chosen in such a way that the highest number of nodes is generated in the contact line region.

In the following sections, we compare the profiles obtained in both the laboratory frame (LF) and the moving frame (MF) by using a uniform grid (UG) or a nonuniform grid (NG). The NG is defined as follows:

$$\Delta x_i = \begin{cases} s + d\tanh\left\{P(-x + x_0 - \frac{w}{2})\right\} & (x < x_0), \\ s + d\tanh\left\{P(x - x_0 - \frac{w}{2})\right\} & (x \geqslant x_0). \end{cases} \tag{15}$$

Here, x_0 and w are the center and width of the region with the largest grid density, respectively, and P controls the steepness of the transition from the coarsest to the finest cell size (see Fig. 2). The constants s and d are defined in terms of the finest and coarsest cell size, $\Delta x_{\min}$ and $\Delta x_{\max}$, respectively, in the following way:

$$s = \frac{\Delta x_{\max} + \Delta x_{\min}}{2}, \qquad d = \frac{\Delta x_{\max} - \Delta x_{\min}}{2}. \tag{16}$$

A scheme of a typical Δx_i function is presented in Fig. 2.

Three UG (UG_1, UG_2 and UG_3) and three NG (NG_1, NG_2 and NG_3) are employed for the analysis of the CF case. The grids UG_4 and NG_4 have a larger domain with $x_{\text{end}} = 100$ and

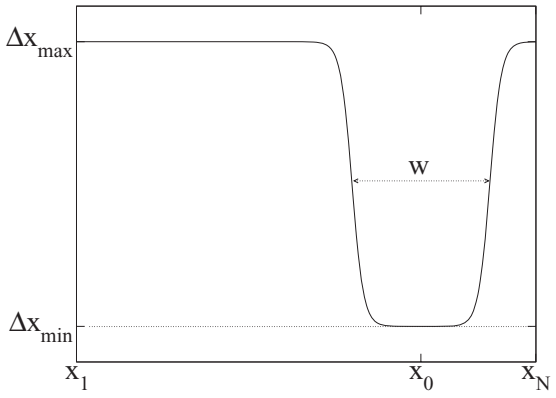

FIG. 2. Scheme of a NG generated by Eq. (15).

TABLE I. Parameters of the uniform grids (UG) and nonuniform grids (NG). Notice that $\Delta x_{\min}$ of each grid NG_j is the Δx employed in UG_j, with $j = 1, 2, 3$, and 4.

	$\Delta x_{\min}$ (10^{-2})	$\Delta x_{\max}$ (10^{-2})	x_0	x_{end}	w	P	N
UG_1	2.5	2.5		23		0	920
UG_2	1.25	1.25		23		0	1840
UG_3	0.3125	0.3125		23		0	7360
UG_4	1.25	1.25		100		0	8000
NG_1	2.5	5	20	23	20	1	713
NG_2	1.25	5	20	23	20	1	1198
NG_3	0.3125	5	20	23	15	1	3193
NG_4	1.25	5	90	100	20	1	4765

they are used to simulate the CV case. The parameters of each mesh are presented in Table I.

IV. CONSTANT FLOW CASE

For the CF configuration, the constant thickness at $x = 0$ is chosen as the scale h_c, thus $h(0) = 1$ (see Fig. 3). At the other boundary, the thickness b of the precursor film is imposed, that is, $h(L) = b$. The first and third derivatives are assumed to be zero at $x = 0, L$. These boundary conditions result in a constant rate inflow that monotonically increases the fluid volume.

In the next subsection, we introduce a few details of how to reduce the full partial differential equation (PDE), Eq. (4), to an ordinary differential equation (ODE). The solution of the ODE is useful to evaluate the accuracy of the solutions obtained by solving the PDE. After that, we proceed with the analysis of the problem by solving the PDE.

A. Reducing the governing PDE to an ODE

As mentioned before, the CF configuration allows a traveling-wave solution. Briefly, to find such a stationary solution in a moving reference frame, we consider $\partial h/\partial t = 0$

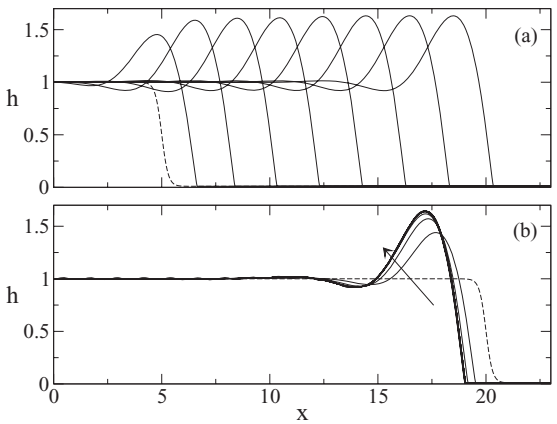

FIG. 3. Evolution of the CF case solved in the (a) laboratory and (b) moving frames. The initial condition (dashed line) is given by Eq. (21), with $c_0 = 5$ and $c_1 = 0.3$. The profiles are for $t = 2$, 4, 6, 8, 10, 12, 14, and 16. The arrow points in the direction of increasing time. Here $G_\perp = 0$ and $b = 10^{-2}$.

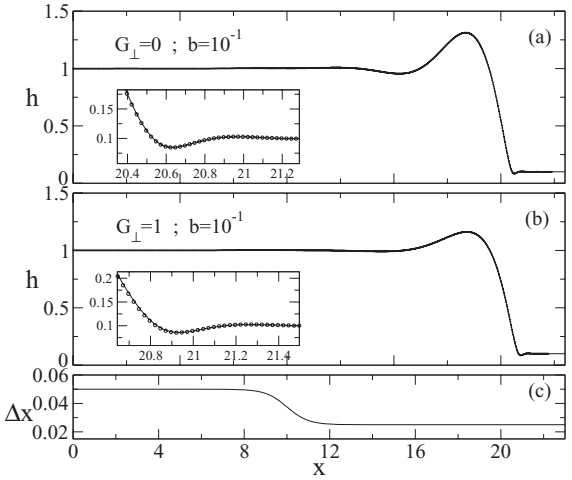

FIG. 4. Thickness profiles at $t = 14$ obtained by employing UG_1-LF (solid line) and NG_1-MF (circles) for $b = 10^{-1}$. (a) $G_\perp = 0$; (b) $G_\perp = 1$; and (c) Δx as a function of x for NG_1 (see Table I).

in Eq. (4) with the scaling x_c defined by

$$x_c = \left(\frac{a^2 h_c}{\sin\alpha}\right)^{1/3}. \tag{17}$$

Then, the first integral of this equation is

$$h_0^3 h_{0,xxx} + h_0^3 - G_\perp h_0^3 h_{0,x} - U_0 h_0 = j, \tag{18}$$

where $h_0(x)$ is the traveling-wave solution. Specular boundary conditions result in

$$j = -b(b+1), \quad U_0 = 1 + b + b^2 \tag{19}$$

(more details can be found in [15]). Interestingly, the expression for $\bar{u}$ simplifies to become

$$\bar{u}(x) = U_0 + j/h_0(x). \tag{20}$$

Notice that this form of $\bar{u}$ says that when the full PDE is solved, and as the profile adopts the asymptotic traveling-wave shape, the maximum of $\bar{u}'$ employed in Eq. (14) corresponds

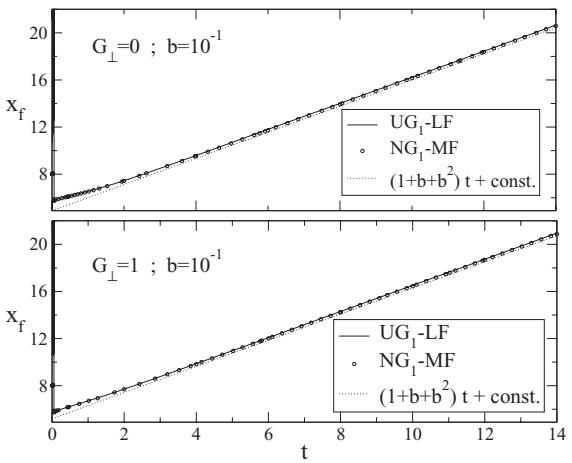

FIG. 5. Front position for the cases presented in Fig. 4. The dashed line represents the phase velocity of the wave, $U = 1 + b + b^2$, given in Eq. (19). Top: $G_\perp = 0$. Bottom: $G_\perp = 1$.

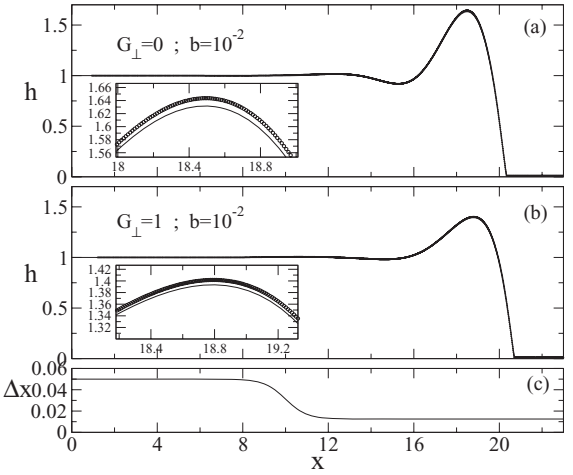

FIG. 6. Thickness profiles obtained with UG_2-LF (solid line) and with NG_2-MF (circles) for $b = 10^{-2}$ at $t = 16$. (a) $G_\perp = 0$; (b) $G_\perp = 1$; and (c) Δx as a function of x for NG_2 (see Table I).

with the maximum of h_0, i.e., the velocity at the bump close to the contact line. The solution of Eq. (18) was employed to measure the accuracy of the solutions computed by solving Eq. (4) in the laboratory frame.

B. Solving the full PDE: Profiles and computing times in laboratory and moving frames

In order to solve the full problem given by Eq. (4), we calculate the evolution from the following initial condition:

$$h_{x,0} = \frac{1-b}{2}\left(1 - \tanh\frac{x - c_0}{c_1}\right) + b, \tag{21}$$

c_0 and c_1 being constants that control the position and width of the transition from 1 to b. The boundary conditions are $h(0,t) = 1$ and $h(L,t) = b$. A typical evolution from the initial state is presented in Fig. 3. The convergence was analyzed to obtain a Δx for which quadratic convergence is assured. In general, $\Delta x = 1.25 \times 10^{-2}$ is enough to obtain a profile that differs from the ODE solution by less than 1%.

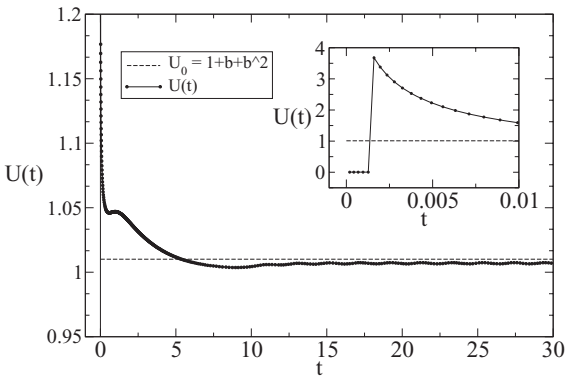

FIG. 7. The velocity $U(t)$ of the moving frame (solid line) asymptotically approaches a value close to the velocity U_0 of the traveling wave (dashed line). The inset shows a zoom of the initial times. Notice that at the first stages, U is set to zero to avoid spurious oscillations. Here, $b = 10^{-2}$.

TABLE II. CPU times (CPUT) for uniform grids in a laboratory frame (UG-LF) and nonuniform grids in a moving frame (NG-MF). F is the ratio of the CPU times for UG-LF and NU-MF.

		Laboratory frame			Moving frame			
b	$G_\perp$	Grid	N	CPUT (h:m:s)	Grid	N	CPUT (h:m:s)	F
10^{-1}	0	UG_1	920	00:02:03	NG_1	713	00:00:33	3.7
	1	UG_1	920	00:01:46	NG_1	713	00:00:34	3.1
	0	UG_2	1840	00:32:32	NG_2	1198	00:03:40	8.9
10^{-2}	0	UG_3	7360	73:32:09	NG_3	3193	49:38:02	1.5
	1	UG_2	1840	00:34:28	NG_2	1198	00:03:18	10.4
	1	UG_3	7360	77:10:50	NG_3	3193	34:27:40	2.2

When solving in the LF, the advancing front at $t = 0$ is positioned close to the origin, as shown in Fig. 3(a). On the contrary, when a MF is employed, it is convenient to place the advancing front close to the right side of the numerical domain, here by setting $c_0 = 20$. This is due to the fact that the advancing front stays at almost the same position when the problem is solved in a MF, moving only slightly at the initial stages of the evolution as shown in Fig. 3(b). In the following numerical experiments, the simulation in the LF is left to run until the advancing front is close to the end of the domain. Then, the thickness profiles $h(x,t)$ and positions of the fronts $x_f(t)$ are compared.

Figure 4 shows profiles for $b = 10^{-1}$ obtained by using UG_1-LF and NG_1-MF for $G_\perp = 0$ and 1 at $t = 14$. There is an excellent agreement even in the most critical region (i.e., the contact line), as shown in the inset.

Figure 5 shows the front positions $x_f(t)$ obtained for the LF and MF, for $G_\perp = 0$ and 1 with $b = 10^{-1}$. For the LF, the calculation of $x_f(t)$ is obtained directly from the simulation. For the MF, the equivalent position in a LF is obtained by adding the displacement of the frame at each temporal step. Figure 5 shows a spurious discrepancy at the beginning that came from the algorithm employed to detect the front as the minimum of the profile.

Figure 6 compares the profiles obtained in both frames for $b = 10^{-2}$ and $G_\perp = 0; 1$. The grids employed were UG_2 for LF and NG_2 for MF. There is good agreement between the profiles; the highest difference is less than 1% at the maximum of the profile. This difference is reduced even more by using the grid NG_3 (not shown for brevity).

Figure 7 shows the evolution of $U(t)$. The simple algorithm defined by Eq. (14) causes U to rapidly approach to the asymptotic value U_0 defined in Eq. (19).

After showing the excellent agreement between the profiles obtained in both frames, now we analyze the computing times consumed in the simulations. The results are presented in Table II.

The first two rows presented in Table II are spreadings with $b = 10^{-1}$. We employ the grids UG_1 in the LF and NG_1 in the MF, for which the ratio of nodes N is $f = 713/920 = 0.7$. When using the NG_1, the simulation speeds up by a factor $F = 3.7$ for $G_\perp = 0$ and $F = 3.1$ for $G_\perp = 1$.

For $b = 10^{-2}$ we employ UG_2 in the MF and NG_2 for the LF, with the corresponding ratio $f = 0.65$. In the MF, the CPU time is reduced by a factor of $F = 8.9$ for $G_\perp = 0$ and $F = 10.4$ for $G_\perp = 1$. The use of lower values of $\Delta x_{\min}$ does not necessarily imply a higher F. For example, when we compare the performance of the algorithm for $b = 10^{-2}$ with

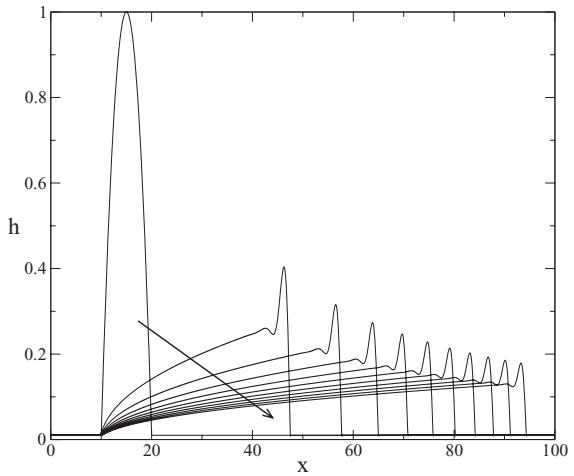

FIG. 8. Thickness profile for UG_4-LF with $\Delta x = 1.25 \times 10^{-2}$ for $t = 0,160,320,\ldots,1600$. The arrow points in the direction of increasing time.

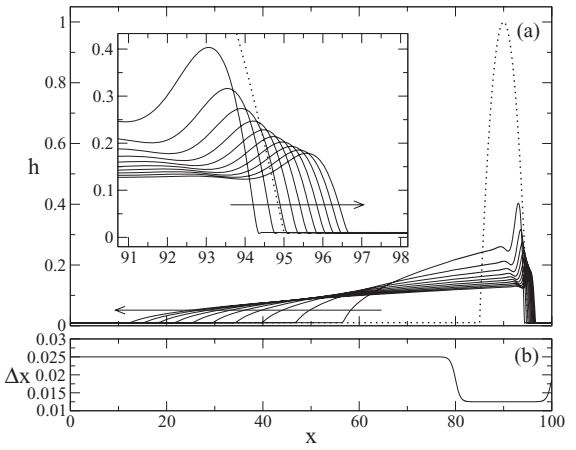

FIG. 9. (a) Thickness profile for NG_4-MF at $t = 0,160,320,\ldots,1600$ (solid lines). The initial condition is represented by the dotted line. The inset shows the evolution of the contact line region. (b) Cell size Δx vs x for NG_4.

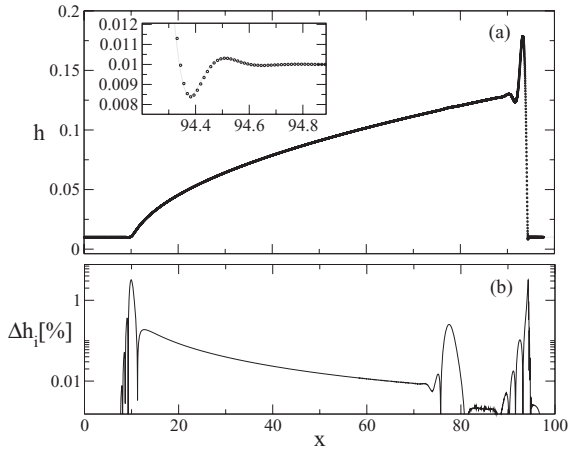

FIG. 10. (a) Comparison of the thickness profiles shown in Fig. 8 (UG_4-LF, dotted line) and in Fig. 9 (NG_4-LF, circles) at $t = 1600$. The inset is a zoom of the advancing contact line. (b) Percentage difference $\delta h_i = 100|h_i^{NG_4} - h_i^{UG_4}|/h_i^{UG_4}$.

the grids UG_3 and NUG_3 ($f = 0.43$), the CPU time ratios for the cases $G_\perp = 0$ and 1 are $F = 1.5$ and 2.2, respectively.

In the next section, we illustrate how both the use of a NG and a MF separately reduce the CPU time by solving the same case in a (i) UG-LF, (ii) NG-LF, and (iii) NG-MF.

V. THE CONSTANT VOLUME PROBLEM

With the aim of testing the proposed algorithm in more general configurations that do not possess traveling-wave solutions, in this section we solve the spreading of a constant volume of fluid on a vertical plane. Here, the action of gravity, capillary, and surface tension compete and the whole profile advances with a nonconstant velocity. The initial profile is a cylindrical cap given by [5]

$$h(x,0) = h_0\left[1 - \left(\frac{2(x - x_a)}{w_0}\right)^2\right], \qquad (22)$$

h_0 and w_0 being the initial thickness and width, respectively, and x_a the position of the apex.

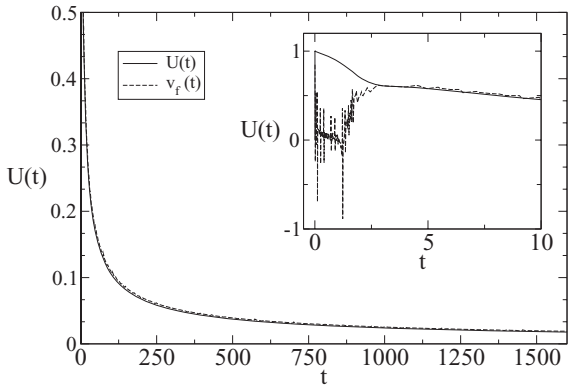

FIG. 11. The velocity $U(t)$ of the moving frame (solid line) for the CV case. After an initial transient stage, shown in the inset, U approaches the velocity of the front $v_f = dx_f/dt$ (dashed line).

TABLE III. Computing times for UG_4-LF, UG_4-MF, and NG_4-MF.

	CPU time (h:m:s)	N
UG_4-LF	4:47:53	8000
UG_4-MF	0:47:49	8000
NG_4-MF	0:21:20	4765

The CV problem does not possess a thickness that remains constant during the spreading, so the scales employed in the CF are not appropriate here. For the CV problem, we define the scales $h_c = x_c = a$ and the time scale is $t_c = 3\mu a/\gamma$. With this scaling, Eq. (4) becomes

$$h_t = -\{h^3[h_{xxx} - \sin\alpha + \cos\alpha\, h_x + U(t)h]\}_x. \qquad (23)$$

The initial state of this case is a cylindrical cap with $h_0 = 1$ and $w_0 = 10$ on a vertical plane, that is, $\alpha = \pi/2$. The precursor film is $b = 10^{-2}$. Figure 8 shows the evolution for UG_4-LF with $\Delta x = 1.25 \times 10^{-2}$. The cell size for the UG_4 was chosen after a convergence analysis in order to assure a solution with an accuracy better than 1%. Figure 9 shows the same case but using a NG_4-MF. As in the CF case, the advancing contact line is placed close to the end of the numerical domain because it almost does not move in the moving frame.

Figure 10(a) shows a good agreement between the thickness profiles obtained by using UG_4-LF and NG_4-MF at $t = 1600$, despite the fact that Δx_{max} of the NG_4 is four times greater than the Δx of the UG_4. The positions x of the NG_4-MF were also calculated in the corresponding LF in order to compare the profiles and the relatives movements (there are no artificial shifts). Figure 10(b) shows that the percentage difference between both profiles is lower than 4% (interpolated values of h were employed for the UG_4-LF).

Figure 11 shows the evolution of $U(t)$ for the CV case. The simple algorithm defined by Eq. (14) causes U to rapidly approach the velocity of the front $v_f = dx_f/dt$. Thus, in the moving frame, the advancing front almost stays in the same place and the most critical zone stays in the densest region of the mesh, as shown in the inset of Fig. 9.

In order to isolate the effects of using a moving mesh and a nonuniform grid, here we compare the computing times of solving the same problem in moving and laboratory frames with the same UG. Table III shows that when solving in the UG-MF, the computing time is six times lower than when a UG-LF is employed. When a NG-LF is employed, the computing time is reduced by a factor of 13.

VI. CONCLUSIONS

An algorithm that reduces the computing time of thin-film flows with moving contact lines is presented. The success of the method rests on two facts. The first is that the region that needs the smaller values of Δx, and smaller temporal step Δt, stays almost in the same place when solved in a moving frame with a velocity $U(t)$. Thus, this region is solved in a quasisteady frame that allows for increasing the temporal step Δt and, consequently, reducing the computing time. The second reason is that a nonuniform grid can be easily implemented, using small cell sizes Δx only in the most critical region.

It is noticeable that in the examples presented, no special effort was needed to design the grid. In fact, the grids employed were not optimal grids, and it is possible to reduce even more the computing time by reducing the number N of nodes without losing precision.

The simplicity of the algorithm enables an easy implementation when other configurations or forces are considered, because all that is needed is to change the expression for the velocity $\bar{u}$ given in Eq. (4). For example, thermocapillary-driven flows on horizontal surfaces can be solved just replacing $G_{\parallel}$ by a constant that takes into account the Marangoni stress and changing h^3 by h^2 in the same term [7,29].

ACKNOWLEDGMENTS

The author is grateful for support from the *Consejo Nacional de Investigaciones Científicas y Técnicas (CONICET-Argentina)*, ANPCyT Grant PICT 2007 No. 872. The author also gratefully acknowledges the comments and suggestions made by J. Diez, D. Campana, and the anonymous referees.

APPENDIX: CONVERGENCE

A comparison of the convergence rates for uniform and nonuniform rates are presented in Fig. 12. The maximum of the thickness profile, $h_{\max}$, is shown as a function of $\Delta x_{\min}$ (for UGs, $\Delta x_{\min} = \Delta x_{\max} = \text{const}$). The use of a UG-LF (squares in the figure) shows a faster approach to the asymptotic value than the use of NG-MF (circles). Nevertheless, in all cases the convergence for UG and NG is quadratic. At first glance, this convergence may be unexpected for NGs. Nevertheless, the NGs employed in this work can be considered as two UGs connected by a NG placed in a noncritical region. Thus, due to the convergence being controlled by the thickness profile at the contact line region, where we have an almost UG, the convergence with Δx is quadratic for our NGs.

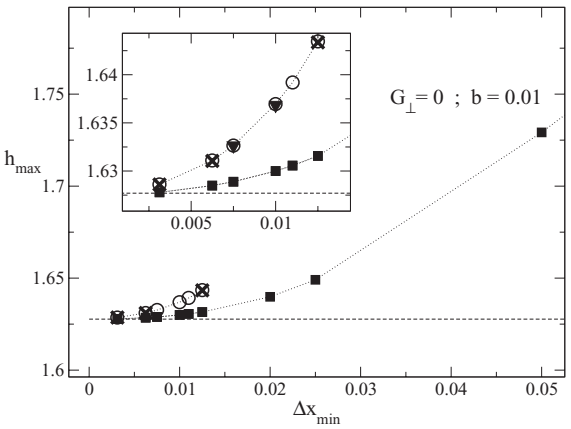

FIG. 12. Convergence rate for different methods: UG-LF ($\Delta x = \Delta x_{\min}$, squares), UG-MF ($\Delta x = \Delta x_{\min}$, triangles), NG-MF ($\Delta x_{\max} = 0.05$, circles), and NG-MF ($\Delta x_{\max} = 0.025$, crosses). The dashed line represents the value of $h_{\max}$ obtained by solving the ODE given by Eq. (18). The inset is a zoom of the data closer to $\Delta x_{\min} = 0$.

The difference in the convergence rates does not come from the use of UGs and NGs, but from solving the problem in a moving frame. Effectively, this fact can be appreciated in Fig. 12, where the cases solved in UG-LF (squares) with $\Delta x = 0.01$ and 0.0075 are also solved in UG-MF (triangles). Notice that the use of a MF causes the points to "jump" from the LF curve to the MF curve.

Finally, the use of two different NGs does not introduce a significant change in the convergence rate. For example, the results obtained by using $\Delta x_{\max} = 0.025$ (crosses) do not show a noticeable difference with the corresponding cases solved with $\Delta x_{\max} = 0.05$ (circles). This reinforces the idea that the convergence is controlled by the region of the grid with smaller values of Δx.

[1] H. Huppert, Nature (London) **300**, 427 (1982).
[2] F. Brochard, Langmuir **5**, 432 (1989).
[3] J. P. Valentino, A. A. Darhuber, S. M. Troian, and S. Wagner, MRS Online Proceedings Library, Vol. 773 (2003), http://journals.cambridge.org/article_S1946427400138059.
[4] H. A. Stone, A. D. Stroock, and A. Ajdari, Annu. Rev. Fluid Mech. **36**, 381 (2004).
[5] J. Gomba, J. Diez, A. G. González, and R. Gratton, Phys. Rev. E **71**, 016304 (2005).
[6] Y. Gotkis, I. Ivanov, N. Murisic, and L. Kondic, Phys. Rev. Lett. **97**, 186101 (2006).
[7] J. M. Gomba and G. M. Homsy, J. Fluid. Mech. **647**, 125 (2010).
[8] A. Oron, S. H. Davis, and S. G. Bankoff, Rev. Mod. Phys. **69**, 931 (1997).
[9] D. Bonn, J. Eggers, J. Indekeu, J. Meunier, and E. Rolley, Rev. Mod. Phys. **81**, 739 (2009).
[10] C. I. Christov, J. Pontes, D. Walgraef, and M. G. Velarde, Comput. Methods Appl. Mech. Eng. **148**, 209 (1997).
[11] L. W. Schwartz and R. R. Eley, J. Colloid Interface Sci. **202**, 173 (1998).
[12] J. A. Diez and L. Kondic, Phys. Rev. Lett. **86**, 632 (2001).
[13] A. L. Bertozzi, G. Grün, and T. P. Witelski, Nonlinearity **14**, 1569 (2001).
[14] L. W. Schwartz and R. V. Roy, Phys. Fluids **16**, 569 (2004).
[15] J. M. Gomba, J. Diez, R. Gratton, A. G. González, and L. Kondic, Phys. Rev. E **76**, 046308 (2007).
[16] J. Diez and L. Kondic, J. Comp. Phys. **183**, 274 (2002).
[17] S. Li and L. Petzold, J. Comp. Phys. **131**, 368 (1997).
[18] Y. Lee, H. Thompson, and P. Gaskell, Comput. Fluids **36**, 838 (2007).
[19] P. H. Gaskell, P. K. Jimack, M. Sellier, and H. M. Thompson, Int. J. Numer. Meth. Fluids **45**, 1161 (2004).
[20] P. H. Gaskell, P. K. Jimack, M. Sellier, H. M. Thompson, and M. C. T. Wilson, J. Fluid Mech. **509**, 253 (2004).
[21] P. H. Gaskell, P. K. Jimack, M. Sellier, and H. M. Thompson, Phys. Fluids **18**, 013601 (2006).
[22] E. O. Tuck and L. W. Schwartz, SIAM Rev. **32**, 453 (1990).
[23] P. G. Lopez, M. J. Miksis, and S. G. Bankoff, Phys. Fluids **9**, 2177 (1997).
[24] L. Kondic and J. Diez, Phys. Rev. E **65**, 045301 (2002).

[25] L. Zhornitskaya, Ph.D. thesis, Duke University, 1999.
[26] L. Zhornitskaya and A. L. Bertozzi, SIAM J. Numer. Anal. **37**, 523 (2000).
[27] A. L. Bertozzi and M. Pugh, Commun. Pure Appl. Math. **49**, 85 (1996).
[28] W. H. Press, S. A. Teukolsky, W. T. Vetterling, and B. P. Flannery, *Numerical Recipes in Fortran 77* (Cambridge University Press, New York, 1992). The routines used in this work are BANDEC and BANBKS.
[29] J. M Gomba, *Optimization of Computing Times in Thin Film Flows with Moving Contact Lines*, talk at the Fifth MIT Conference on Computational Fluid and Solid Mechanics Focus: Advances in CFD (MIT Press, Cambridge, MA, 2009).